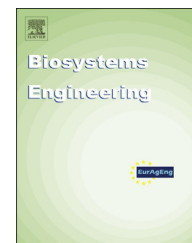


Available online at [www.sciencedirect.com](http://www.sciencedirect.com)

ScienceDirect

journal homepage: [www.elsevier.com/locate/issn/15375110](http://www.elsevier.com/locate/issn/15375110)

## Research Paper

# Feasibility study on Huanglongbing (citrus greening) detection based on WorldView-2 satellite imagery



Xiuhua Li <sup>a,b,c,d</sup>, Won Suk Lee <sup>d,\*</sup>, Minzan Li <sup>c</sup>, Reza Ehsani <sup>e</sup>,  
Ashish R. Mishra <sup>e</sup>, Chenghai Yang <sup>f</sup>, Robert L. Mangan <sup>g</sup>

<sup>a</sup> College of Electrical Engineering, Guangxi University, Nanning 530004, China

<sup>b</sup> Guangxi Experiment Centre of Science and Technology, Nanning 530004, China

<sup>c</sup> Key Laboratory of Modern Precision Agriculture Integration Research, MOE, China Agricultural University, Beijing 100083, China

<sup>d</sup> Department of Agricultural & Biological Engineering, University of Florida, Gainesville, FL 32611, United States

<sup>e</sup> Citrus Research and Education Center, University of Florida, 700 Experiment Station Road, Lake Alfred, FL 33850, United States

<sup>f</sup> USDA-ARS, Southern Plains Agricultural Research Center, College Station, TX 77845, United States

<sup>g</sup> USDA-ARS, Subtropical Horticulture Research Station, 13601 Old Cutler Rd., Miami, FL 33158, United States

## ARTICLE INFO

## Article history:

Received 20 February 2014

Received in revised form

20 January 2015

Accepted 30 January 2015

Published online

## Keywords:

Huanglongbing

Library construction

Satellite multispectral image

Supervised classification

Huanglongbing (HLB) is a devastating citrus disease worldwide, without known cure. Since this disease shows visible symptoms on newly developed canopies, remote sensing methods based on spectral principles are considered as an effective tool. To explore a fast way to monitor HLB in large citrus groves, a satellite multispectral (MS) image with a 2-m resolution acquired by WorldView-2 was studied to evaluate its capability on HLB detection. Ground truth was conducted and two spectral libraries were constructed. Library 1 was based on RTK GPS locations, and Library 2 was combined with prior knowledge from the ground spectral features. To compare with the classification accuracy of previous work using airborne spectral images, the same classification methods were carried out. In the satellite MS image, Library 2 had higher average overall accuracy, higher Kappa coefficient, and higher producer's and user's accuracies than Library 1, indicating Library 2 which combined with prior knowledge was more effective. Mahalanobis distance had the highest overall accuracy of 81% and a Kappa coefficient of 0.464 with Library 2. The accuracy comparison between the satellite MS image and the airborne spectral images showed that the satellite MS image had the highest average producer's accuracy with Library 2, followed by the airborne MS image and the satellite MS image with Library 1, indicating that construction of an effective library was the most important step, and that the satellite MS image with a proper spatial resolution showed good potential to be a better choice than the airborne spectral image.

© 2015 IAGrE. Published by Elsevier Ltd. All rights reserved.

\* Corresponding author.

E-mail addresses: [wlee@ufl.edu](mailto:wlee@ufl.edu), [wlee32608@gmail.com](mailto:wlee32608@gmail.com) (W.S. Lee).  
<http://dx.doi.org/10.1016/j.biosystemseng.2015.01.009>

1537-5110/© 2015 IAGrE. Published by Elsevier Ltd. All rights reserved.

## 1. Introduction

Huanglongbing (HLB), which is also known as the citrus greening or yellow dragon disease, is one of the most serious citrus diseases in the world. Once a tree is infected, there is no known cure, and it should be removed and destroyed to reduce further infection. It has devastated millions of hectares of citrus crops worldwide. HLB was presumed to originate in Asia in the late 19th century, and then was widely spread to Africa several decades ago (Batool, Iftikhar, Mughal, Khan, & Jaskani, 2007). Several years ago, it was also found in two of the largest citrus growing regions in the world - São Paulo, Brazil, and Florida, USA (Bové, 2006).

Polymerase chain reaction (PCR) method is the most definitive way to confirm HLB disease in leaves, but this molecular biochemical method is time consuming and costly. Since this disease exhibits obvious symptoms on new leaves, especially after the middle infection stage, a visual examination by experienced workers is commonly used to detect the disease. But this ground scouting method is time-consuming and labour-intensive for large groves. In recent years, some ground-based spectral sensors for other applications have been designed and reported (Gonzalez-Mora, Vallespi, Dima, & Ehsani, 2010; Mishra, Karimi, Ehsani, & Albrigo, 2011; Pydipati, 2004; Qin, Burks, Ritenour, & Bonn, 2009), trying to assist workers to efficiently manage different diseases, but they still have made little improvement on the speed to cover large groves.

Satellite spectral imagery can easily cover hundreds of hectares, and their spatial resolution has improved from dozens of metres decades ago to several metres, or even sub-metre (Mulla, 2012). It has been widely studied and used for agricultural applications, such as estimating nitrogen deficiencies in sugar beet (Seelan, Laguette, Casady, & Seielstad, 2003) and maize (Bausch & Khosla, 2010), leaf area for vines (Johnson, Roczen, Youkhana, Nemani, & Bosch, 2003), and wheat yield (Doraiswamy, Moulin, Cook, & Stern, 2003; Labus, Nielsen, Lawrence, Engel, & Long, 2002).

Studies on monitoring plant disease based on satellite imagery have also been reported. Mirik et al. (2011) used Landsat 5 Thematic Mapper (TM) images to detect the wheat streak mosaic disease, and their accuracies were between 89 and 99% when compared to field observations with a maximum likelihood classifier. Bhattacharya and Chattopadhyay (2013) combined EO-1 satellite imagery with surface weather data, and explored an effective way to predict mustard rot disease in three stages. Apan, Held, Phinn, and Markley (2004) evaluated classification accuracies of 40 spectral vegetation indices derived from EO-1 Hyperion imagery to discriminate 'orange rust' (*Puccinia kuehnii*) disease in sugarcane, and reported that several newly formulated indices consisting of visible and near-infrared bands and the moisture-sensitive band (1660 nm) yielded improved results.

The traditional normalised difference vegetation index (NDVI) is a well-established mechanism for identifying vegetation pixels. It relies on the principle that the chlorophyll in living plant material strongly absorbs visible light, and strongly reflects NIR light.

Green normalised difference vegetation index (GNDVI) has proved more sensitive than NDVI when predicting

chlorophyll-a (Gitelson, Kaufman, & Merzlyak, 1996), and has been widely used to measure plant chlorophyll content, tissue nitrogen (Bell et al., 2004), and biomass (Hunt et al., 2011; Moges et al., 2005). It has been also adopted to detect diseases in soybean (Vigier, Pattey, & Strachan, 2004) and winter wheat (Yuan et al., 2013).

Spectral reflectance information in the red edge region could also infer chlorophyll content variations. Horler, Dockray, and Barber (1983) found that the red edge measurements were valuable for chlorophyll status and leaf area index assessment, and were particularly suitable for early stress detection. Zarco-Tejada and Miller (1999) conducted a land cover classification study using red edge spectral information acquired by a compact airborne spectrographic imager. The producer's and user's accuracies were about 68.6% and 61.2%, respectively. Researchers have also shown that a Red to Red-Edge comparison (simple ratio index, SRI) is better able to discriminate between healthy trees and those impacted by disease.

Previous studies (Li et al., 2012; Li, Lee, Wang, Ehsani, & Yang, 2014) analysed the difference between ground-based spectra of healthy and HLB infected canopies, and the results showed obvious differences in the reflectance at visible and NIR bands, and at REP (red edge position). Several airborne hyperspectral and multispectral images were also acquired to detect the HLB more efficiently and yielded detection results of about 65% with minimum distance method. In order to further explore a more economic and larger coverage method, satellite spectral imagery with comparable spatial resolution was considered as an alternative tool. In this research, a WorldView-2 multispectral image was adopted to evaluate its potential usage for HLB disease detection, since WorldView-2 provides one of the highest spatial resolutions (1.85 m at nadir) so far available among all the satellite multispectral products. Thus, the objectives of this study were to: 1) analyse the satellite spectral difference between HLB and healthy canopies; 2) apply supervised classification methods to explore the possibility for HLB detection; 3) compare detection accuracy with that from airborne images in a previous study.

## 2. Materials and methods

### 2.1. Image acquisition

The experiment area was two orange blocks at the southwest corner of a commercial citrus grove (Southern Garden), located in the Hendry County, Florida, USA. This area was completely planted with the citrus variety *Valencia*, and was partly infected by HLB disease. At the time of image acquisition, oranges with green or yellowish green colour were present on the trees. The tree spacing was 3.0–3.7 m in the row, and the row spacing was 7.0–8.5 m.

The multispectral (MS) and hyperspectral (HS) airborne images in the previous studies (Li et al., 2012) were acquired by two prototype systems (developed by Yang, Everitt, Davis, and Mao (2003) and Yang (2010), as shown in Fig. 1a), at 2:30 p.m. local time on December 3, 2010. The spatial resolutions were 0.5 m and 1.0 m, respectively.

In order to best match the airborne images, WorldView-2 satellite images with the closest acquisition time and spatial

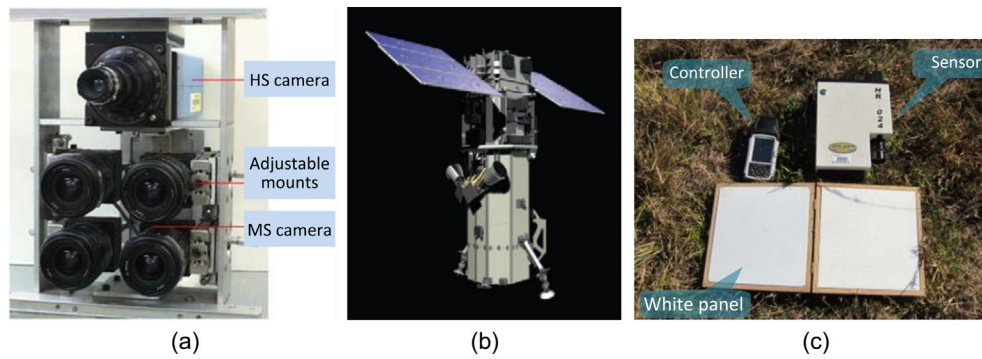


**Fig. 1 – Equipment for the satellite and aerial imaging: (a) airborne HS and MS imaging systems (Yang, 2010), (b) WorldView-2 satellite, and (c) HR-1024 handheld spectrometer along with a white panel for ground spectral measurements.**

resolution were selected for this study. The WorldView-2 (Fig. 1b), which was launched in October 2009, is the first high-resolution 8-band multispectral commercial satellite, with an operating altitude of 770 km (Digital Globe, 2013). The spatial resolution of the satellite panchromatic and MS images are 0.5 and 2 m, respectively. The WorldView-2 satellite images which contained a panchromatic and a MS image were acquired at 11:28 a.m. local time, December 20, 2010. The sun zenith angle was  $41.2^\circ$ , and azimuth angle was  $164.4^\circ$  (in a clockwise direction from the north). The satellite zenith and azimuth angles were  $31.8^\circ$  and  $206.3^\circ$ , respectively, and so the satellite was looking northeast. The image was taken in an off nadir angle of  $27.9^\circ$ , and was resampled with nearest neighbour which kept the original information of each pixel. The satellite images of the study area are shown in Fig. 2. Basic information of these four images is listed in Table 1.

## 2.2. Ground truth investigation

Two kinds of ground truth investigation were conducted in the study area in Fig. 2: one was a rough investigation, and the other was an accurate investigation. In the rough investigation, all trees were scouted by ground inspection crews, and suspicious diseased trees with HLB symptoms were marked out by recording their GPS locations with a positioning accuracy of 1–3 m. Some of the scouted-as-diseased/healthy trees were chosen for accurate investigation, including PCR test, ground spectral measurement and RTK GPS position recording (with a static horizontal accuracy of 3 mm by HiPer XT, Topcon, Livermore, CA, USA). PCR test is a common and reliable lab method to confirm infection status. The ground reflectance of the healthy and diseased tree leaves were measured by a handheld spectrometer (HR-1024, Spectra Vista

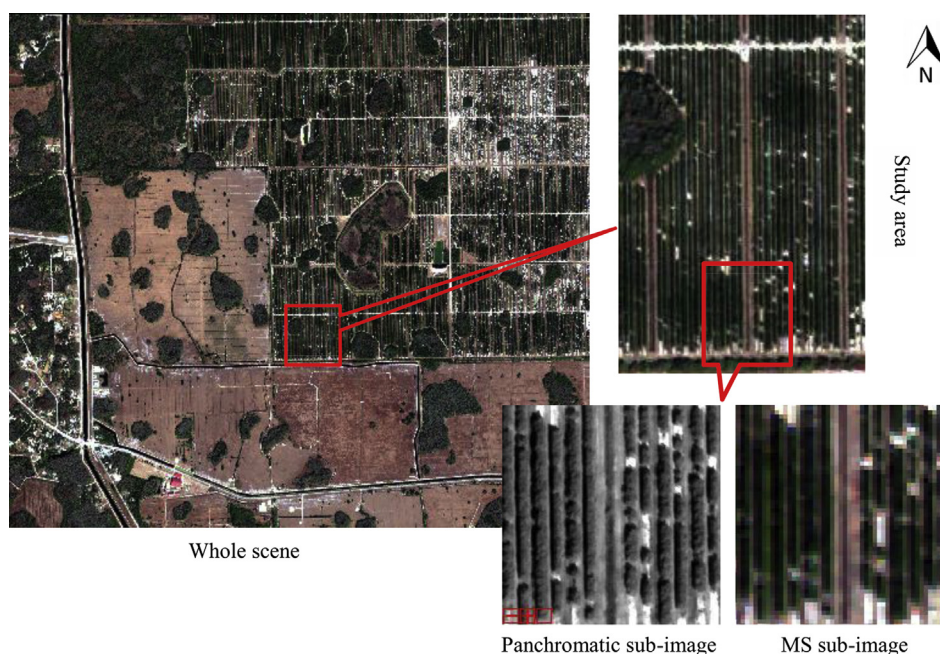


**Fig. 2 – WorldView-2 satellite images of the study area (Southern Garden citrus grove).**



Corporation, Poughkeepsie, NY, USA, shown in Fig. 1c). During the reflectance measurement, the instrument was put about 0.2 m above the target leaf, and the lens axis was perpendicular to the leaf surface, with a field of view of 4°. In the accurate investigation, leaf samples were divided into two classes according to their symptom visibility and their PCR test results, as shown in Table 3. Leaves in HEA\_PCR\_N class had no symptoms and showed negative in PCR test; leaves in S\_PCR\_P class had obvious symptoms and PCR positive sign. Since most of the samples in the accurate investigation were distributed in the sub-image area in Fig. 2, the subsequent analysis and classifications were mainly focused in this sub-image. The sample quantities for each class were also listed in Table 3. More details about the ground truth investigation have been described in the previous study (Li et al., 2012).

### 2.3. Satellite image analysis

SA\_MS was used for image classification, because it had original digital numbers (DN). The satellite MS image analysis was mainly carried out with ENVI software (version 4.8, ITT VSI, White Plains, NY, USA). Figure 3 shows the main processing and analysing procedures, including ground truth investigation, image correction, image spectra analysis and image classification.

The ground truth contained the ground spectrum and locations. Image correction included geometric correction, radiometric correction and spectral correction. Pixel spectral differences between healthy and HLB samples were analysed and vegetation indices (VIs) were further calculated and analysed. Several supervised classification methods were adopted in image classification.

#### 2.3.1. Satellite image pre-processing

**2.3.1.1. Radiometric and geometric correction.** The satellite images were geo-referenced by the image provider to UTM N17 projection with the datum of WGS-84, the same projection as that of the airborne images. Sensor corrections, geometric corrections and radiometric corrections were also conducted by the image provider, with a standard procedure which applied to every image product. Sensor corrections included corrections for internal detector geometry, optical distortion, scan distortion, and line-rate variations. Geometric corrections removed spacecraft orbit position and altitude uncertainty, Earth rotation and curvature, and panoramic distortion. Since the original DN values should not be altered when doing quantitative classifications, nearest neighbour was chosen when resampling the image because it ensured unaltered DN values. Radiometric corrections included relative radiometric response between detectors, non-responsive detector fill and conversion for absolute radiometry (Digital Globe, 2010).

**2.3.1.2. Spectral radiance and reflectance conversion.** The pixel data or DN values in the satellite images provided by the image provider were unique to WorldView-2. In order to conduct further comparison with imagery from other sensors, and calculate proper VIs, Top-of-atmosphere spectral radiance and reflectance should be further converted from the DN values for the satellite images.

Top-of-atmosphere spectral radiance was defined as the spectral radiance entering the telescope aperture at the WorldView-2 altitude of 770 km. Equation (1) was used to convert the DN values in each satellite image band to top-of-atmosphere spectral radiance (Digital Globe, 2010):

$$L_{\lambda_{\text{Pixel, Band}}} = \frac{K_{\text{Band}} \cdot q_{\text{Pixel, Band}}}{\Delta\lambda_{\text{Band}}} \quad (1)$$

where  $L_{\lambda_{\text{Pixel, Band}}}$  is image pixels in spectral radiance ( $\text{W} \cdot \text{m}^{-2} \cdot \text{sr}^{-1} \cdot \mu\text{m}^{-1}$ ),  $q_{\text{Pixel, Band}}$  is radiometrically corrected image pixels, or the DN values,  $K_{\text{Band}}$  and  $\Delta\lambda_{\text{Band}}$  are the absolute radiometric calibration factor ( $\text{W} \cdot \text{m}^{-2} \cdot \text{sr}^{-1} \cdot \text{count}^{-1}$ ) and the effective bandwidth ( $\mu\text{m}$ ) for a given band, respectively;  $K_{\text{Band}}$  and  $\Delta\lambda_{\text{Band}}$  are given in the image metadata.

By ignoring atmospheric effects, the surface reflectance could be calculated from the top-of-atmosphere spectral radiance with the following equation:

$$\rho_{\lambda_{\text{Pixel, Band}}} = \frac{L_{\lambda_{\text{Pixel, Band}}} \cdot d_{\text{ES}}^2 \cdot \pi}{E_{\text{sun}, \lambda_{\text{Band}}} \cdot \cos(\theta_s)} \quad (2)$$

where  $\rho_{\lambda_{\text{Pixel, Band}}}$  is the target diffuse spectral reflectance,  $E_{\text{sun}, \lambda_{\text{Band}}}$  is the solar spectral irradiance at specific band,  $\theta_s$  is the solar zenith angle, and  $d_{\text{ES}}$  is the Earth-Sun distance.  $E_{\text{sun}, \lambda_{\text{Band}}}$  was given by Digital Globe,  $\theta_s$  could be found in the satellite imagery metadata and  $d_{\text{ES}}$  could be calculated by the following equations:

$$g = 357.529 + 0.98560028 \cdot (JD - 2451545.0) \quad (3)$$

$$d_{\text{ES}} = 1.00014 - 0.01671 \cos(g) - 0.00014 \cdot \cos(2g) \quad (4)$$

where  $JD$  is the Julian Day corresponding to the image acquisition time, and  $g$  is in degrees.

The corrected spectral signatures for a healthy pixel are shown in Fig. 4.

**2.3.1.3. Ground truth location unification.** In this research, most of the infected trees were at the early and middle stages of the disease, and most of the infection areas were much smaller than a 2-m-pixel, and were randomly scattered. In the accurate ground investigation, the RTK receiver was placed at the left side of the trees (shown as diamonds for HEA\_PCR\_N and circles for S\_PCR\_P in Fig. 5) to record the tree positions rather than the specific infection canopy. Since the trees were more than 7 m wide and 4 m tall, forming hedge rows, the exact infection areas for each infected tree couldn't be determined by these GPS records. So each tree was studied as a whole, and the tree centres were taken as sampling references. Accordingly, all the original GPS records were horizontally moved to the row centre (shown as crosshairs in Fig. 5).

**2.3.1.4. Image background masking.** In order to reduce the background influence from grass, shadow, bare ground, etc., an image mask for the tree canopy was built using support vector machine (SVM) method, the same as used with the airborne images in the previous study (Li et al., 2012). Since the satellite images were taken at 11:28 a.m., with the sun's zenith angle of 41.2°, each tree row had an observable sunlit side (east side) and a shadowed side (west side), as shown in Fig. 5. In order to reduce the light influence on classification results, those two sides were masked out as well.

**Table 1 – Information for the satellite images and compared airborne images.**

Image	Description	Imaging sensor	Acquisition time	Altitude	Spatial resolution	Spectral resolution
SA_PAN	Satellite panchromatic image	WorldView-2	11:28 a.m., Dec. 20, 2010	770 km at nadir	0.5 m	One panchromatic band from 450 to 800 nm with centre wavelength of 625 nm
SA_MS	Satellite multispectral image				2.0 m	Eight bands (Table 2)
AB_MS	Airborne multispectral image	Experimental imaging system	2:39 p.m., Dec.3, 2010	1220 m	0.5 m	Four bands at 450, 550, 650, and 830 nm, with the bandwidth of 40 nm
AB_HS	Airborne hyperspectral image	developed by Yang et al. (2003) and Yang (2010)	2:30 p.m., Dec.3, 2010	910 m	1.0 m	128 bands from 457.2 to 921.7 nm with an interval of 3.6 nm

### 2.3.2. Spectral feature analysis

2.3.2.1. *Library constructions.* For image classification, especially with supervised classification methods, the method to construct an effective library was vital. Due to the relatively low image spatial resolution, two different procedures were carried out to build different spectral libraries for both healthy and HLB classes.

When building Library 1, the right half of the sub-image (the right side of the ditch) was used as the training area, and the left half as the testing area. All the samples in the training area were considered as training samples. Only the centre pixel of each training sample in HEA\_PCR\_N and S\_PCR\_P classes was collected into the healthy and HLB libraries.

Since the GPS positions only pointed at the tree centres instead of the specific infected canopies, another procedure was implemented to build Library 2. Library 2 was based upon the ground reflectance features between the healthy and HLB class found in the previous study (Li et al., 2012), i.e., the healthy class had lower reflectance in the visible bands, and higher reflectance in the NIR bands. In Library 2, we first expanded the Healthy and HLB sample sets by including neighbouring pixels which had great possibility to be the healthy or HLB pixels, then we used prior knowledge to select pixels with typical features to form the training set for each class. The other samples were left as testing samples. In this procedure, since most of the trees had at least four pixels in the MS image, four neighbouring pixels for each sample (with an area of 4 × 4 m) in S\_PCR\_P and HEA\_PCR\_N were collected to form two datasets. Their reflectance in green and NIR1 wavebands were then exported to the n-D Visualizer, as shown in Fig. 6. According to the ground reflectance features

for each class, pixels with higher reflectance in the green band and lower reflectance in the NIR band were manually picked out as an HLB library, and the healthy library was picked out in the opposite way.

2.3.2.2. *Vegetation indices calculation.* Since WorldView-2 has two NIR bands, one red-edge band, and five common visible bands, three types of widely used VIs were adopted in this research: NDVI, SRI, and GNDVI. All the VIs were calculated from the MS reflectance image. According to the different bands used in those VIs, a total of nine VIs were calculated, as shown in Table 4.

### 2.3.3. Image classification methods

Classification methods are commonly applied to the first several principal component images which are derived from the original image, especially for hyperspectral images that have a large numbers of spectral bands. But since the principal component conversion is only based on the statistical significance of the spectra, some small objects with unique spectra might manifest in the last several principal component images, which would probably be discarded, causing unexpected loss of valuable information (Dhodhi, Saghri, Ahmad, & Ul-mustafa, 1999). Thus, in this research, since the MS image has only 8 bands in total, all of them were directly used in the image classification process to keep the maximum amount of useful information.

In order to compare the classification accuracy with the airborne images, the same supervised classification methods and spectral mapping methods were used, including parallelepiped, minimum distance (MinDist), Mahalanobis distance (MahaDist), spectral angle mapper (SAM), spectral information divergence (SID), mixture tuned matched filtering (MTMF). More detailed description of these methods has been given in the previous study (Li et al., 2012). For each method, the error matrix was used to calculate the user's and producer's accuracies, the overall accuracy, and Kappa coefficient.

**Table 2 – Band information of the WorldView-2 satellite MS image.**

Band name	Centre wavelength (nm)	Minimum lower band edge (nm)	Maximum upper band edge (nm)
MS1 (Coastal)	425	400	450
MS2 (Blue)	480	450	510
MS3 (Green)	545	510	580
MS4 (Yellow)	605	585	625
MS5 (Red)	660	630	690
MS6 (Red Edge)	725	705	745
MS7 (NIR1)	835	770	895
MS8 (NIR2)	950	860	1040

## 3. Results and discussion

### 3.1. Library spectral signature comparison

The mean spectra for each class in Library 1 and 2 are shown in Fig. 7, the numbers in parentheses are the sample quantities. Means test was also applied between healthy and HLB

**Table 3 – Classification information for different samples. In the class column, “HEA” stands for “healthy”, “PCR” stands for “polymerase chain reaction”, “P” stands for “positive”, and “N” stands for “negative”.**

Class	Sample numbers in sub-image	Sample source	Symptom	PCR test result
HEA_PCR_N	18	Healthy tree	Asymptomatic	Negative
S_PCR_P	71	HLB infected tree	Symptomatic	Positive

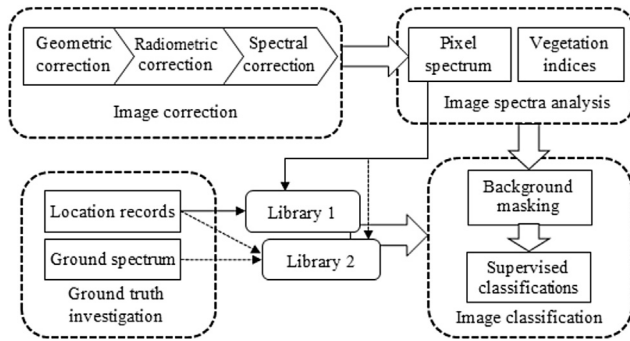


**Fig. 3 – Block diagram of satellite imagery analysis procedure.**

class to examine whether there were significant differences (shown in Table 5). For Library 1, the reflectance of the HLB library showed little difference from that of the healthy library in the visible range, but was somewhat lower in the NIR range. The means test for Library 1 showed no significant difference for any band between the two classes ( $p\text{-value} \geq 0.05$ ). Usually, less significant difference in the library indicates more difficulty and less accuracy in the subsequent classification.

The similar features in Library 1 were mainly caused by:

- (1) Most of the HLB infection areas were smaller than one pixel in the early and middle infection stages, the spectral features of diseased canopies could be diluted by nearby healthy canopy in the same pixel, thus causing similar neutral spectral features;
- (2) The HLB pixels in Library 1 which were simply collected from tree centres might not contain infected canopies; this further made the differences in Library 1 much narrower.
- (3) At the time of the experiment, the trees had some yellow-green citrus fruit on them, and the fruit could

also influence the canopy spectrum and dilute the healthy and diseased spectral features.

In Fig. 7b, the two classes in Library 2 showed much greater differences in the visible and NIR range. The means test also showed significant differences at each band except for Band 4 (B4) and Band 6 (B6), and the spectral features were identical with the ground truth.

### 3.2. Vegetation indices comparison

Means tests were also conducted to compare the differences for vegetation indices between healthy and HLB classes (Tables 6 and 7). The results showed that, for all the VIs, the healthy class had higher average values and lower sample variances than the HLB class for both libraries, but Library 1 had much narrower differences between each class. A t-test was also conducted for each VI to further explore the significance of differences. It showed that, in Library 1, NDVI1, NDVI2, NDVI\_RE, SRI2 and GNDVI2 have significant difference at a significance level of 0.01; in Library 2, all the indices showed significant differences.

### 3.3. Image classification result

The MinDist method was recommended in the previous study, and in this study, its classification result for the satellite image is given in Fig. 8 as an example. Because the rough ground truth had too much positioning error, and its infection status was not confirmed by PCR test either, only accurate ground truth was used as the referenced true value. In the accurate ground truth, only S\_PCR\_P class, which had obvious symptoms, was used as the true values for HLB infected trees, and HEA\_PCR\_N class was used for healthy trees to count the classification accuracy. Samples which were used to build the libraries were considered as the training samples, and the rest were the testing samples. When counting the accuracy, a whole tree was considered as the smallest unit, i.e., if one pixel from four close pixels (which was considered as a tree)

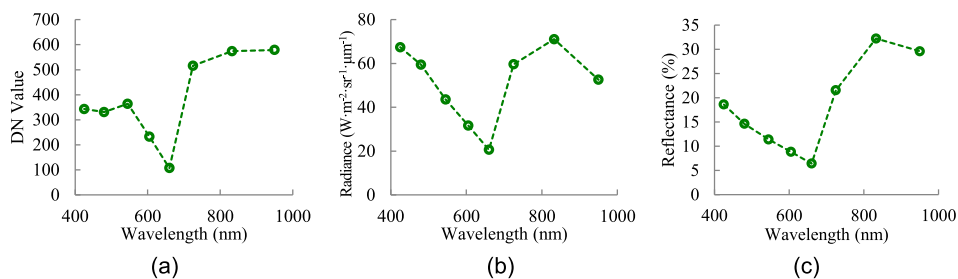


**Fig. 4 – Different types of spectral signatures for a healthy pixel: (a) DN Value, (b) top-of-atmosphere radiance, and (c) top-of-atmosphere reflectance.**

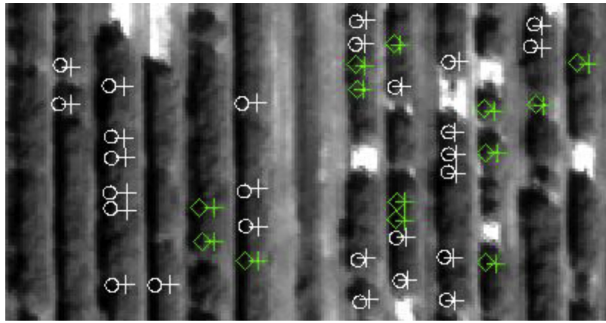


**Fig. 5 – GPS records correction. Diamonds and circles represent the original GPS locations of HEA\_PCR\_N and S\_PCR\_P respectively, crosshairs represent the corrected GPS locations; green represents HEA\_PCR\_N, and white represents S\_PCR\_P.**

was classified as HLB infected, the whole tree was classified as HLB infected. This assumption indicated that a tolerance of one pixel was allowed between ground truth location and classified result.

The producer's and user's accuracies for both HEA\_PCR\_N and S\_PCR\_P classes in the testing set are listed in Table 8. The overall accuracy and Kappa coefficient were also calculated and listed in Table 9. Several points were found in the results:

- (1) The average producer's accuracies for S\_PCR\_P and HEA\_PCR\_N were 63% and 70% with Library 1, 64% and 76% with Library 2, respectively. The average user's accuracies for those two classes were 35% and 88% with Library 1, 41% and 89% with Library 2, respectively. The overall accuracies ranged from 65%–73% with Library 1, and 65%–81% with Library 2. The Kappa coefficients were mostly less than 0.3 with Library 1, but half of them were higher than 0.35 with Library 2. For each indicator, Library 2 had higher accuracy than Library 1, indicating a better performance. This also showed that

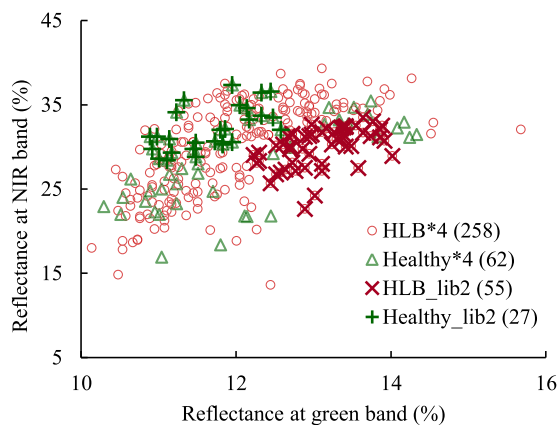


**Fig. 6 – Library 2 construction in the n-D Visualizer: '△' and '○' represent the universal datasets for healthy and HLB class; '×' and '+' represent the healthy and HLB libraries selected according to the ground spectral features.**

**Table 4 – Vegetation indices and their calculation formulae.**

VI	Calculation formulae		
NDVI	NDVI1	NDVI2	NDVI_RE
	$\frac{NIR1 - Red}{NIR1 + Red}$	$\frac{NIR2 - Red}{NIR2 + Red}$	$\frac{RedEdge - Red}{RedEdge + Red}$
SRI	SRI1	SRI2	SRI_RE
	$\frac{NIR1}{Red}$	$\frac{NIR2}{Red}$	$\frac{RedEdge}{Red}$
GNDVI	GNDVI1	GNDVI2	GNDVI_RE
	$\frac{NIR1 - Green}{NIR1 + Green}$	$\frac{NIR2 - Green}{NIR2 + Green}$	$\frac{RedEdge - Green}{RedEdge + Green}$

the library building procedure combined with prior knowledge was more effective.

- (2) The accuracies in HEA\_PCR\_N were lower than in S\_PCR\_P, especially for the user's accuracy. This was mainly caused by the unbalanced sample populations between those two classes.
- (3) Among the six classification methods, MahaDist had the highest overall accuracy of 81% and Kappa coefficient of 0.464 with Library 2, and this was in accordance with the conclusion of the previous study on the airborne spectral images (Li et al., 2012).
- (4) Although Library 1 had an overall accuracy of 69%, which showed moderate performance, its average Kappa coefficient was only 0.257, indicating poor accordance with the ground truth, so it was not recommended in this classification.
- (5) The classification methods based on different vegetation indices had no obvious advantages over those based on the reflectance bands.

### 3.4. Detection accuracy comparison

Since the same ground truth and classification methods were used in the previous study on airborne images (Li et al., 2012), the detection accuracy (here referring to the producer's accuracy of HLB) in each image was compared and the result is shown in Fig. 9. The average producer's accuracy for each image is also present as horizontal lines in the plot. The airborne image used only one kind of library which was constructed from the tree centre pixels, like Library 1. From the plot, we had those following conclusions:

- 1) The satellite MS image with Library 2 had the highest average accuracy of 76%, this mainly benefited from its library construction method which used prior knowledge.
- 2) The satellite MS image with Library 1 had an average accuracy of 70%, very close to that of the airborne MS image which was 71%. Those two images were both applied with the same kind of libraries, so the result indicated that their difference on spatial resolution had very limited influence on the classification results in this case.
- 3) The airborne HS image had the lowest accuracy (62%) among all images, and this probably resulted from the obvious distortion existed in the immature geometry correction.
- 4) Not only did the satellite MS image have the highest average accuracy using Library 2, but also it had greater similarity of results among all the methods compared to







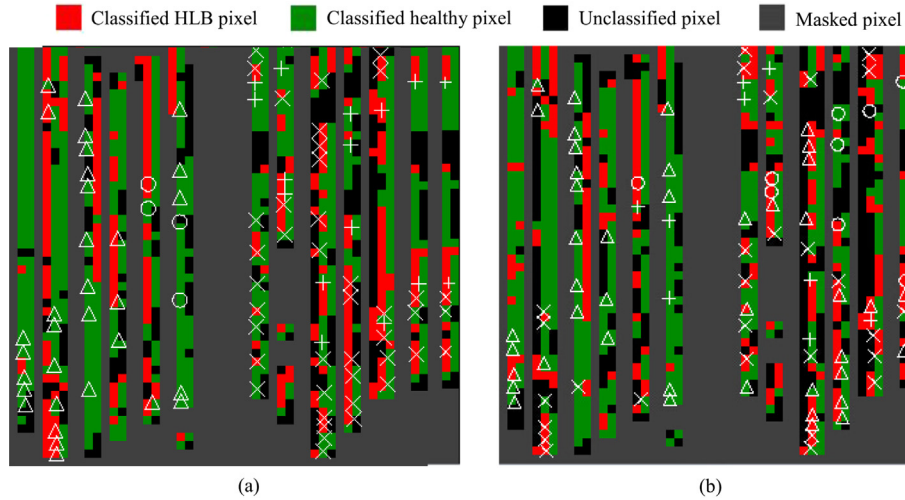


**Fig. 8 – Classification results by MinDist method: (a) classified with Library 1, and (b) classified with Library 2. “+” and “o” represent healthy samples in the training and testing sets, respectively; “x” and “Δ” represent HLB infected samples in the training and testing sets, respectively.**

knowledge from the ground spectral features, the spectral difference between the HLB and healthy classes was obviously wider.

In the classification result, Library 2 had an average overall accuracy of 74%, and Kappa coefficient of 0.333. For each indicator (also including the producer's and user's accuracy), Library 2 had higher accuracy than Library 1, indicating a better performance. This also showed that the library building

procedure combined with prior knowledge was more effective. Among the six classification methods, Mahalanobis distance had the highest overall accuracy of 81% and Kappa coefficient of 0.464 with Library 2, and this was accordance with the conclusion of the previous study on airborne spectral images (Li et al., 2012). Library 1, which had very low Kappa coefficient, indicated poor accordance with the ground truth, and was not recommended for classification. The

**Table 8 – The producer's and user's accuracies for each method with different libraries in the testing sets. The testing ground truth populations were 36 for Library 1, and 52 for Library 2. In the classification method column, NDVI1\_MinDist represented MinDist method carried out on the NDVI1 band, and similar for GNDVI1\_MinDist and SRI1\_MinDist. Vis\_MinDist was MinDist method carried out on an image composed from all VI bands.**

Library	Classification method	Producer's accuracy		User's accuracy	
		HEA_PCR_N	S_PCR_P	HEA_PCR_N	S_PCR_P
Library 1	Parallelepiped	72%	63%	33%	90%
	MinDist	56%	76%	37%	87%
	MahaDist	72%	69%	37%	91%
	SAM	56%	72%	33%	86%
	SID	56%	68%	30%	86%
	MTMF	61%	72%	35%	88%
	NDVI1_MinDist	61%	69%	33%	88%
	GNDVI1_MinDist	67%	68%	34%	89%
	SRI1_MinDist	67%	70%	36%	89%
	Vis_MinDist	67%	75%	40%	90%
	Average accuracy	63%	70%	35%	88%
Library 2	Parallelepiped	61%	79%	42%	89%
	MinDist	67%	80%	46%	90%
	MahaDist	67%	85%	52%	91%
	SAM	67%	77%	43%	90%
	SID	61%	82%	46%	89%
	MTMF	61%	66%	31%	87%
	NDVI1_MinDist	56%	77%	38%	87%
	GNDVI1_MinDist	67%	79%	44%	90%
	SRI1_MinDist	61%	69%	33%	88%
	Vis_MinDist	72%	66%	35%	90%
	Average accuracy	64%	76%	41%	89%

**Table 9 – The overall accuracy and Kappa coefficient for each method with two libraries.**

Method	Library 1		Library 2	
	Overall accuracy	Kappa coefficient	Overall accuracy	Kappa coefficient
Parallelepiped	65%	0.248	75%	0.343
MinDist	72%	0.266	78%	0.403
MahaDist	70%	0.305	81%	0.464
SAM	69%	0.219	75%	0.366
SID	65%	0.177	78%	0.381
MTMF	70%	0.259	65%	0.202
NDVI1_MinDist	67%	0.230	73%	0.283
GNDVI1_MinDist	67%	0.253	76%	0.384
SRI1_MinDist	70%	0.283	67%	0.230
Vis_MinDist	73%	0.331	67%	0.276
Average	69%	0.257	74%	0.333

classification methods based on different vegetation indices had no obvious advantages over those based on the reflectance bands.

The accuracy comparison between the satellite MS image and the airborne spectral images in the previous study showed that the satellite MS image with Library 2 had the highest average producer's accuracy of 76%, followed by the airborne MS image and the satellite MS image with Library 1, the last was the airborne HS. This order reflected the importance of the following factors for HLB remote sensing with similar spatial resolution: library > geometric correction (which directly influenced the library accuracy) > spectral resolution. The smaller variation in accuracies between different methods in the satellite image also indicated a more stable performance than the airborne images. All the results indicated that satellite MS images with proper spatial resolution have good potential to be an alternative choice to airborne spectral images to monitor HLB infected trees.

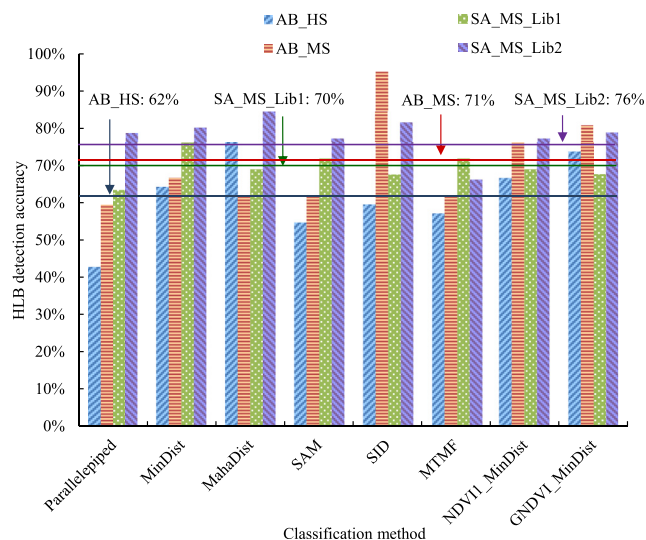


**Fig. 9 – Comparison of the producer's accuracy of HLB for each method in different images, where AB\_HS means airborne hyperspectral image, AB\_MS means airborne multispectral image, SA\_MS\_Lib1 represents satellite multispectral image with Library 1, and SA\_MS\_Lib2 represents satellite multispectral image with Library 2.**

Further study with more comprehensive investigation of ground truth is suggested, such as: (1) specific infected canopy areas should be identified; (2) infection levels (including infection size, infection degree, etc.) of each tree should also be taken into account; (3) the infection status of every tree in the research area should be confirmed by PCR test.

## Acknowledgements

The authors would like to thank Dr. Ce Yang, Dr. Asish Skaria, Dr. Ferhat Kurtulmus, Mr. Anurag Katti and Mr. John Simmons in the Precision Agriculture Laboratory, Agricultural and Biological Engineering Department, University of Florida for their kind support and assistance on the ground truth experiment, and statistical analysis. This study was supported by the Florida Department of Citrus, the China High Technology Research, Development Research Fund (2013AA102303), 948 Project (2011-G32), the National Natural Science Foundation of China (31401290), and Guangxi Experiment Centre of Science and Technology (YXKT2014003).

## REFERENCES

- Apan, A., Held, A., Phinn, S., & Markley, J. (2004). Detecting sugarcane "orange rust" disease using EO-1 hyperion hyperspectral imagery. *International Journal of Remote Sensing*, 25(2), 489–498.
- Batool, A., Iftikhar, Y., Mughal, S. M., Khan, M. M., & Jaskani, M. J. (2007). Citrus greening disease – a major cause of citrus decline in the world – a review. *HortScience (Prague)*, 34(4), 159–166.
- Bausch, W. C., & Khosla, R. (2010). QuickBird satellite versus ground-based multi-spectral data for estimating nitrogen status of irrigated maize. *Precision Agriculture*, 11, 274–290.
- Bell, G. E., Howell, B. M., Johnson, G. V., Raun, W. R., Solie, J. B., & Stone, M. L. (2004). Optical sensing of turfgrass chlorophyll content and tissue nitrogen. *HortScience*, 39(5), 1130–1132.
- Bhattacharya, B. K., & Chattopadhyay, C. (2013). A multi-stage tracking for mustard rot disease combining surface meteorology and satellite remote sensing. *Computers and Electronics in Agriculture*, 90, 35–44.
- Bové, J. M. (2006). Huanglongbing: a destructive, newly-emerging, century-old disease of citrus. *Journal of Plant Pathology*, 88(1), 7–37.

- Dhodhi, M. K., Saghri, J. A., Ahmad, I., & Ul-mustafa, R. (1999). D-ISODATA: a distributed algorithm for unsupervised classification of remotely sensed data on network of workstations. *Journal of Parallel and Distributed Computing*, 59(2), 280–301.
- Doraiswamy, P. C., Moulin, S., Cook, P. W., & Stern, A. (2003). Crop yield assessment from remote sensing. *Photogrammetric Engineering & Remote Sensing*, 69(6), 665–674.
- Digital Globe. (2010). *Technical note: Radiometric use of WorldView-2 imagery*. Access link [http://www.digitalglobe.com/sites/default/files/Radiometric\\_Use\\_of\\_WorldView-2\\_Imagery%20%281%29.pdf](http://www.digitalglobe.com/sites/default/files/Radiometric_Use_of_WorldView-2_Imagery%20%281%29.pdf).
- Digital Globe. (2013). *Datasheet: WorldView-2 spacecraft information and specifications*. Access link [http://www.digitalglobe.com/sites/default/files/DG\\_WorldView2\\_DS\\_PROD.pdf](http://www.digitalglobe.com/sites/default/files/DG_WorldView2_DS_PROD.pdf).
- Gitelson, A. A., Kaufman, Y. J., & Merzlyak, M. N. (1996). Use of a green channel in remote sensing of global vegetation from EOS-MODIS. *Remote Sensing of Environment*, 58, 289–298.
- Gonzalez-Mora, J., Vallespi, C., Dima, C. S., & Ehsani, R. (2010). HLB detection using hyperspectral radiometry. In *10th ICPA Proceedings*. <http://www.andrew.cmu.edu/user/jlibby/robotany/Gonzalez-Mora-2010.pdf>.
- Horler, D. N. H., Dockray, M., & Barber, J. (1983). The red edge of plant leaf reflectance. *International Journal of Remote Sensing*, 4(2), 273–288.
- Hunt, E. R., Hively, W. D., McCarty, G. W., Daughtry, C. S. T., Forrestal, P. J., Kratochvil, R. J., et al. (2011). NIR-green-blue high-resolution digital images for assessment of winter cover crop biomass. *GIScience & Remote Sensing*, 48(1), 86–98.
- Johnson, L. F., Roczen, D. E., Youkhana, S. K., Nemani, R. R., & Bosch, D. F. (2003). Mapping vineyard leaf area with multispectral satellite imagery. *Computers and Electronics in Agriculture*, 38(1), 33–44.
- Labus, M. P., Nielsen, G. A., Lawrence, R. L., Engel, R., & Long, D. S. (2002). Wheat yield estimates using multi-temporal NDVI satellite imagery. *International Journal of Remote Sensing*, 23(20), 4169–4180.
- Li, X., Lee, W. S., Li, M., Ehsani, R., Mishra, A. R., Yang, C., et al. (2012). Spectral difference analysis and airborne imaging classification for citrus greening infected trees. *Computers and Electronics in Agriculture*, 83, 32–46.
- Li, H., Lee, W. S., Wang, K., Ehsani, R., & Yang, C. (2014). 'Extended spectral angle mapping (ESAM)' for citrus greening disease detection using airborne hyperspectral imaging. *Precision Agriculture*, 15, 162–183.
- Mirik, M., Jones, D. C., Price, J. A., Workneh, F., Ansley, R. J., & Rush, C. M. (2011). Satellite remote sensing of wheat infected by wheat streak mosaic virus. *Plant Disease*, 95(1), 4–12.
- Mishra, A., Karimi, D., Ehsani, R., & Albrigo, L. G. (2011). Evaluation of an active optical sensor for detection of Huanglongbing (HLB) disease. *Biosystems Engineering*, 110(3), 302–309.
- Moges, S. M., Raun, W. R., Mullen, R. W., Freeman, K. W., Johnson, G. V., & Solie, J. B. (2005). Evaluation of green, red, and near infrared bands for predicting winter wheat biomass, nitrogen uptake, and final grain yield. *Journal of Plant Nutrition*, 27(8), 1431–1441.
- Mulla, D. J. (2012). Twenty five years of remote sensing in precision agriculture: key advances and remaining knowledge gaps. *Biosystems Engineering*, 1–14.
- Pydipati, R. (2004). *Evaluation of classifiers for automatic disease detection in citrus leaves using machine vision*. MS thesis. Gainesville, FL: University of Florida.
- Qin, J., Burks, T. F., Ritenour, M. A., & Bonn, W. G. (2009). Detection of citrus canker using hyperspectral reflectance imaging with spectral information divergence. *Journal of Food Engineering*, 93(2), 183–191.
- Seelan, S. K., Laguetta, S., Casady, G. M., & Seielstad, G. A. (2003). Remote sensing applications for precision agriculture: a learning community approach. *Remote Sensing of Environment*, 88, 157–169.
- Vigier, B. J., Pattey, E., & Strachan, I. B. (2004). Narrowband vegetation indexes and detection of disease damage in soybeans. *IEEE Geoscience and Remote Sensing Letters*, 1(4), 255–259.
- Yang, C. (2010). *An airborne four-camera imaging system for agricultural applications*. ASABE Paper No. 1008855. St. Joseph: Michigan.
- Yang, C., Everitt, J. H., Davis, M. R., & Mao, C. (2003). A CCD camera-based hyperspectral imaging system for stationary and airborne applications. *Geocarto International*, 18(2), 71–80.
- Yuan, L., Zhang, J., Wang, K., Loraamm, R., Huang, W., Wang, J., et al. (2013). Analysis of spectral difference between the foreside and backside of leaves in yellow rust disease detection for winter wheat. *Precision Agriculture*, 14(5), 495–511.
- Zarco-tejada, P. J., & Miller, J. R. (1999). Land cover mapping at BOREAS using red edge spectral parameters from CASI imagery. *Journal of Geophysical Research*, 104(D22), 27921–27933.